

# Lattice BGK Model for Incompressible Navier–Stokes Equation

Zhaoli Guo,<sup>\*</sup> Baochang Shi,<sup>†</sup> and Nengchao Wang<sup>†</sup>

*<sup>\*</sup>National Laboratory of Coal Combustion, and Department of Computer Science, Huazhong University of Science and Technology, Wuhan 430074, People's Republic of China; and <sup>†</sup>Department of Mathematics, Huazhong University of Science and Technology, Wuhan 430074, People's Republic of China*  
E-mail: sbchust@public.wuhan.cngh.com

Received May 10, 1999; revised February 28, 2000

---

Most of the existing lattice Boltzmann BGK models (LBGK) can be viewed as compressible schemes to simulate incompressible fluid flows. The compressible effect might lead to some undesirable errors in numerical simulations. In this paper a LBGK model without compressible effect is designed for simulating incompressible flows. The incompressible Navier–Stokes equations are exactly recovered from this incompressible LBGK model. Numerical simulations of the plane Poiseuille flow, the unsteady 2-D shear decaying flow, the driven cavity flow, and the flow around a circular cylinder are performed. The results agree well with the analytic solutions and the results of previous studies. © 2000 Academic Press

*Key Words:* Lattice BGK method; Incompressible Navier–Stokes equation.

---

## 1. INTRODUCTION

The Lattice Boltzmann BGK (LBGK) method is a new numerical scheme for simulating viscous compressible flows in the subsonic regime [2]. In recent years, LBGK has achieved great success in simulations of fluid flows and in modeling physics in fluids. Through multiscaling expansion [7], the compressible Navier–Stokes equations can be recovered from the lattice Boltzmann BGK equation on the assumptions that (i) the Mach number is small, and (ii) the density varies slowly. Therefore, theoretically the LBGK model can only be used to simulate compressible flows in the incompressible limit. When used for incompressible flows, it must be viewed as an artificial compressible method for the incompressible Navier–Stokes equations. In such circumstances, the LBGK solutions might depart from the direct solutions of the incompressible Navier–Stokes equations [14]; at least part of the departures might be attributable to the effects of the compressibility of the LBGK model. Some efforts have been made to reduce or eliminate such errors [7, 9, 13, 22]. However, most of these existing incompressible LBGK models can be used only to simulate steady

flows. By neglecting terms of higher order Mach number in the equilibrium density distribution function, He and Luo [9] proposed an incompressible LBGK model in which the distribution function is of pressure representation. From the model, the incompressible Navier-Stokes equations in artificial compressible form can be derived. He's model can be used for both incompressible steady and unsteady flows. However, before the model is used, the average pressure of the flow must be specified in advance. In some cases, especially in practical problems, the average pressure is not known or cannot be prescribed precisely. Furthermore, when used to simulate unsteady incompressible flows, the model requires an additional condition,  $T \gg L/c_s$  ( $T$  and  $L$  are characteristic time and length, respectively), to neglect the artificial compressible effect.

Considering the significance of the incompressible Navier-Stokes equations in theory and applications, it is necessary to establish a LBGK model which can exactly model the incompressible Navier-Stokes equations in general. It is well known that the small Mach number limit is equivalent to the incompressible limit, so it is possible to set up a LBGK model which can properly model the incompressible Navier-Stokes equations only with the small Mach number limit. In this paper such an incompressible LBGK model is proposed. The rest of the paper is organized as follows. In Section 2, the 2-D incompressible LBGK model is designed. In Section 3, numerical results are performed to test the incompressible LBGK model. The simulations include the steady Poiseuille flow, the unsteady decaying shear flow, the driven cavity flow, and flow around a circular cylinder. Section 4 summarizes the results and concludes the paper.

## 2. 2-D INCOMPRESSIBLE LBGK MODEL

In this section, we will propose a 9-bit LBGK model in two-dimensional space. The approach can also be used to develop other incompressible LBGK models in either two- or three-dimensional space.

### 2.1. *d2q9 LBGK Model*

The velocity directions of the d2q9 LBGK model [17] are defined as

$$\mathbf{e}_i = \begin{cases} (0, 0) & i = 0 \\ (\cos[(i-1)\pi/2], \sin[(i-1)\pi/2]) & i = 1, 2, 3, 4 \\ \sqrt{2}(\cos[(i-5)\pi/2 + \pi/4], \sin[(i-5)\pi/2 + \pi/4]) & i = 5, 6, 7, 8. \end{cases} \quad (2.1)$$

The evolution equation of the density distribution function reads

$$f_i(\mathbf{x} + c\mathbf{e}_i \Delta t, t + \Delta t) - f_i(\mathbf{x}, t) = -\frac{1}{\tau} [f_i(\mathbf{x}, t) - f_i^{(0)}(\mathbf{x}, t)], \quad (2.2)$$

where  $c = \Delta x / \Delta t$ ,  $\Delta x$ , and  $\Delta t$  are the lattice grid spacing and the time step, respectively;  $\tau$  is the dimensionless relaxation time; and  $f_i^{(0)}(\mathbf{x}, t)$  is the equilibrium density distribution function, which is determined by

$$f_i^{(0)}(\mathbf{x}, t) = \omega_i \rho + \rho s_i(\mathbf{u}(\mathbf{x}, t)), \quad (2.3)$$

where

$$s_i(\mathbf{u}) = \omega_i \left[ 3 \frac{(\mathbf{e}_i \cdot \mathbf{u})}{c} + 4.5 \frac{(\mathbf{e}_i \cdot \mathbf{u})^2}{c^2} - 1.5 \frac{|\mathbf{u}|^2}{c^2} \right] \quad (2.4)$$

with the weight coefficient

$$\omega_i = \begin{cases} \frac{4}{9} & i = 0 \\ \frac{1}{9} & i = 1, 2, 3, 4 \\ \frac{1}{36} & i = 5, 6, 7, 8. \end{cases}$$

The velocity in the above equilibrium distribution function is required to be small; i.e.,  $|\mathbf{u}|/c \approx M \ll 1$ , where  $M$  is the Mach number. The fluid density  $\rho$  and velocity  $\mathbf{u}$  are obtained from the density distribution function  $f_i(\mathbf{x}, t)$ :

$$\rho = \sum_i f_i \quad (2.5)$$

$$\rho \mathbf{u} = \sum_i c \mathbf{e}_i f_i. \quad (2.6)$$

The mass and momentum equations can be derived from the model via multiscaling expansion as

$$\frac{\partial \rho}{\partial t} + \nabla \cdot (\rho \mathbf{u}) = 0 \quad (2.7)$$

$$\frac{\partial(\rho \mathbf{u})}{\partial t} + \nabla \cdot (\rho \mathbf{u} \mathbf{u}) = -\nabla p + \nu [\nabla^2(\rho \mathbf{u}) + \nabla(\nabla \cdot (\rho \mathbf{u}))], \quad (2.8)$$

where  $p = c_s^2 \rho$  is the pressure,  $c_s = c/\sqrt{3}$  is the sound speed, and  $\nu = (2\tau - 1)c^2 \Delta t/6$  is the kinematic viscosity. Clearly, the mass and momentum equations are exactly the same as the compressible Navier–Stokes equations if the density variation is small enough.

## 2.2. Incompressible d2q9 LBGK Model

The d2q9 LBGK model described in the above section requires two conditions: (i) small Mach number and (ii) small density variation. That is, the model is only appropriate for compressible flows in incompressible limit; the incompressible Navier–Stokes equations cannot be recovered properly. In this section, we will give a novel incompressible LBGK model from which the incompressible Navier–Stokes equations can be exactly recovered with the small Mach number limit.

The discrete velocity directions of the model are the same as those of the d2q9 model, and a new type of distribution function  $g_i(\mathbf{x}, t)$  is introduced with the equilibrium distribution function  $g_i^{(0)}(\mathbf{x}, t)$  defined by

$$g_i^{(0)} = \begin{cases} -4\sigma \frac{p}{c^2} + s_0(\mathbf{u}) & i = 0 \\ \lambda \frac{p}{c^2} + s_i(\mathbf{u}) & i = 1, 2, 3, 4 \\ \gamma \frac{p}{c^2} + s_i(\mathbf{u}) & i = 5, 6, 7, 8, \end{cases} \quad (2.9)$$

where  $\sigma$ ,  $\lambda$ , and  $\gamma$  are parameters satisfying

$$\begin{aligned} \lambda + \gamma &= \sigma \\ \lambda + 2\gamma &= \frac{1}{2}. \end{aligned}$$

The distribution function satisfies the following conservation laws:

$$\sum_{i=0}^8 g_i = \sum_{i=0}^8 g_i^{(0)} \quad (2.10)$$

$$\sum_{i=0}^8 c\mathbf{e}_i g_i = \sum_{i=0}^8 c\mathbf{e}_i g_i^{(0)}. \quad (2.11)$$

The evolution equation of the system is

$$g_i(\mathbf{x} + c\mathbf{e}_i \Delta t, t + \Delta t) - g_i(\mathbf{x}, t) = -\frac{1}{\tau} (g_i(\mathbf{x}, t) - g_i^{(0)}(\mathbf{x}, t)). \quad (2.12)$$

The velocity and pressure of flow are given by

$$\mathbf{u} = \sum_{i=1}^8 c\mathbf{e}_i g_i \quad (2.13)$$

$$p = \frac{c^2}{4\sigma} \left[ \sum_{i=1}^8 g_i + s_0(\mathbf{u}) \right]. \quad (2.14)$$

Through multiscaling expansion, the incompressible Navier-Stokes equations can be derived from this incompressible LBGK model as (see the Appendix for details)

$$\nabla \cdot \mathbf{u} = 0 \quad (2.15)$$

$$\frac{\partial \mathbf{u}}{\partial t} + \nabla \cdot (\mathbf{u}\mathbf{u}) = -\nabla p + \nu \nabla^2 \mathbf{u}, \quad (2.16)$$

where the kinematic viscosity is determined by

$$\nu = \frac{(2\tau - 1)}{6} \frac{(\Delta x)^2}{\Delta t}. \quad (2.17)$$

### 3. NUMERICAL RESULTS

To test the incompressible LBGK model proposed in the above section, numerical simulations of the steady plane Poiseuille flow with pressure boundary condition, the unsteady 2-D shear decaying flow, the driven cavity flow with  $\text{Re} = 400, 1000, 2000$ , and  $5000$  and the flow around a circular cylinder with  $\text{Re} = 10, 20, 40$ , and  $82.67$  are performed. In the simulations, the parameters of the incompressible LBGK model are taken as  $\sigma = 5/12$ ,  $\lambda = 1/3$ , and  $\gamma = 1/12$ . The distribution function  $g_i$  is initialized by setting to equal  $g_i^{(0)}$  for all nodes at  $t = 0$ . For boundary conditions, the extrapolation scheme proposed by Chen *et al.* [3] is used. The original scheme uses second-order extrapolation, which is consistent with LBGK methods. However, we found that the second-order extrapolation scheme has poor stability for higher Reynolds numbers. Therefore, we used the second-order extrapolation scheme for boundary conditions in simulating the Poiseuille flow, the shear decaying flow, and the flow around a circular cylinder with  $\text{Re} = 10, 20$ , and  $40$ , but used the first-order extrapolation scheme for the flow around a circular cylinder with  $\text{Re} = 82.67$  and the driven cavity flow with different Reynolds numbers considered for the sake of stability.

### 3.1. Steady Plane Poiseuille Flow

A steady plane Poiseuille flow with pressure boundary conditions is defined in the region  $\{(x, y) \mid 0 \leq x \leq 2, 0 \leq y \leq 1\}$  with the initial and boundary conditions

$$\begin{aligned} u(x, y, 0) &= v(x, y, 0) = 0; \quad p(x, y, 0) = p_0; \\ u(x, 0, t) &= u(x, 1, t) = v(x, 0, t) = v(x, 1, t) = 0; \\ p(0, y, t) &= p_{\text{in}}; \quad p(1, y, t) = p_{\text{out}}, \end{aligned}$$

where  $p_0 = 0.5(p_{\text{in}} + p_{\text{out}})$ , and  $p_{\text{in}}$  and  $p_{\text{out}}$  are the pressure maintained at the entrance and the exit, respectively. The Poiseuille flow has an analytic solution,

$$\begin{aligned} u(x, y, t) &= \frac{\Delta p}{4\nu} y(1-y) \\ v(x, y, t) &= 0 \\ p(x, y, t) &= p_{\text{in}} - \frac{\Delta p}{2} x, \end{aligned} \tag{3.1}$$

where  $\Delta p = p_{\text{in}} - p_{\text{out}}$ .

The parameters used in the simulations are:  $\Delta x = 1/16$ ,  $\nu = 1.0$ ,  $p_{\text{in}} = 1.1$ ,  $p_{\text{out}} = 1.0$ . The lattice size is  $16 \times 32$ . To reach the steady state, a number of iterations are performed. The criterion of steady state is

$$\frac{\sum_{ij} |u_{ij}^{(n+1)} - u_{ij}^{(n)}|}{\sum_{ij} |u_{ij}^{(n+1)}|} \leq 5.0 \times 10^{-9},$$

where  $u_{ij}^n = u(x_i, y_j, n\Delta t)$ . Several different values of  $\tau$  are used in the simulations. With the fixed kinematic viscosity  $\nu$ , the corresponding time steps are determined by Eq. (2.17). It should be pointed out that the profiles of  $u$  along different horizontal lines are almost the same, and the profiles of pressure  $p$  along different vertical lines are also almost the same. Figure 1 shows profiles of the horizontal component of velocity,  $u$ , at the mid-width of the channel,  $x = 1.0$ , and the pressure,  $p$ , at the mid-height of the channel,  $y = 0.5$ . In all the simulations, the vertical component of the velocity,  $v$ , are found to be smaller than  $10^{-10}$ .

We can see that the simulation results of the velocity profiles are of parabolic shape along the channel, and the pressure distribution is linear along the channel.

### 3.2. Unsteady Decaying Shear Flow

The unsteady decaying shear flow has an analytic solution,

$$\begin{aligned} u(x, y, t) &= A \\ v(x, y, t) &= B \cos(kx - kAt) e^{-k^2 \nu t} \\ p(x, y, t) &= p(t), \end{aligned} \tag{3.2}$$

where the constants  $A$ ,  $B$ ,  $k$ ,  $\nu$ , and  $p(t)$  are chosen as  $A = B = k = \nu = 1.0$ ,  $p(t) = p_0 + 0.01 \sin(20\pi t)$ , and  $p_0 = 3.0$  is the average pressure. The domain is defined in the region  $\{(x, y) \mid 0 \leq x \leq 2\pi, 0 \leq y \leq 0.16\pi\}$ . The initial and boundary conditions are implemented according to the analytic solution given by Eqs. (3.2).

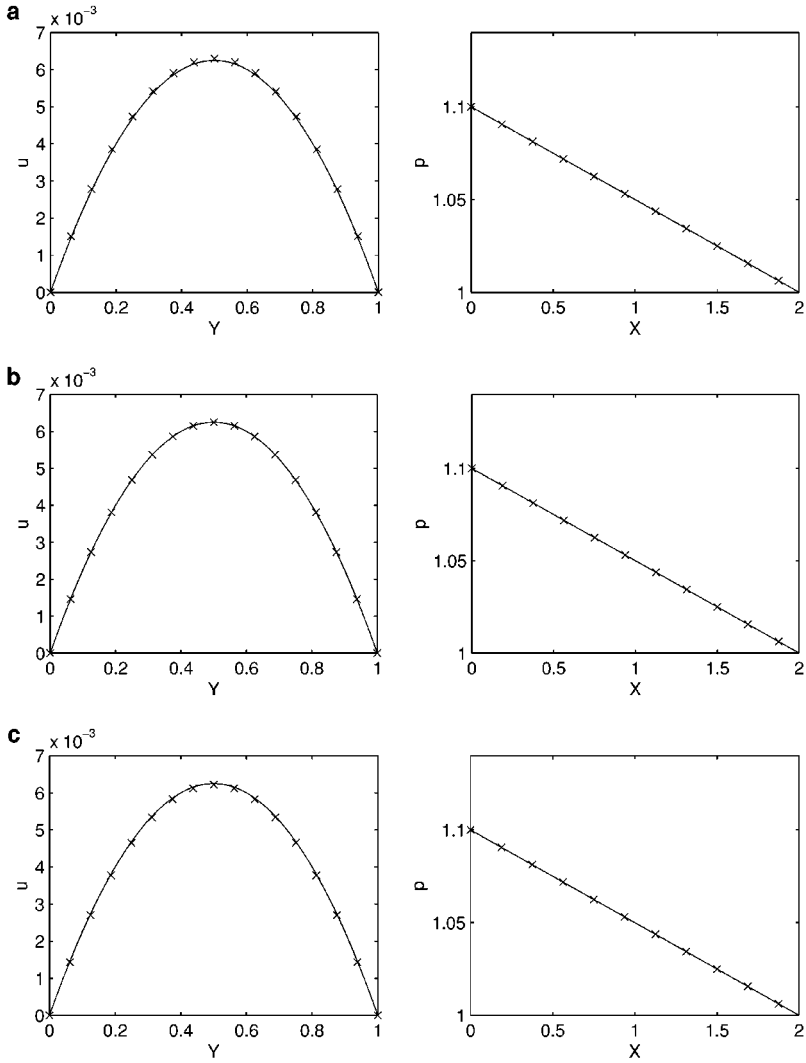


**FIG. 1.** Profiles of velocity  $u$  (left), at the mid-width of the channel ( $x = 1.0$ ), and pressure  $p$  (right), at the mid-height of the channel ( $y = 0.5$ ), in steady plane Poiseuille flow with different relaxation times. Solid lines: analytic solutions.  $\times$ : Simulation results. (a):  $1/\tau = 0.8$ ; (b):  $1/\tau = 1.0$ ; (c):  $1/\tau = 1.2$ .

In the simulation, the lattice size is fixed at  $8 \times 100$ . Data at several different times are measured with fixed relaxation time  $\tau$  such that  $1/\tau = 0.95$ . We observed that in the simulation, the relative global errors of the horizontal component of the velocity,  $u$ , are of order  $10^{-4}$ , and the profiles of the vertical component of the velocity,  $v$ , are similar for different values of  $y$ . Figure 2 shows the simulation results of the vertical component of velocity,  $v$ , at  $y = 0.08\pi$ . It shows that the simulation results agree well with the analytic solution.

To compare with the existing incompressible LBGK model, the relative global error of  $u$  and  $v$  at different times in the simulation are also measured, as listed in Table I. The relative global error is given by

$$\|e(u)\|^2 = \frac{\sum_{i,j} (u_{ij}^{(n)} - \bar{u}_{ij}^{(n)})^2}{\sum_{i,j} (\bar{u}_{ij}^{(n)})^2}, \quad (3.3)$$

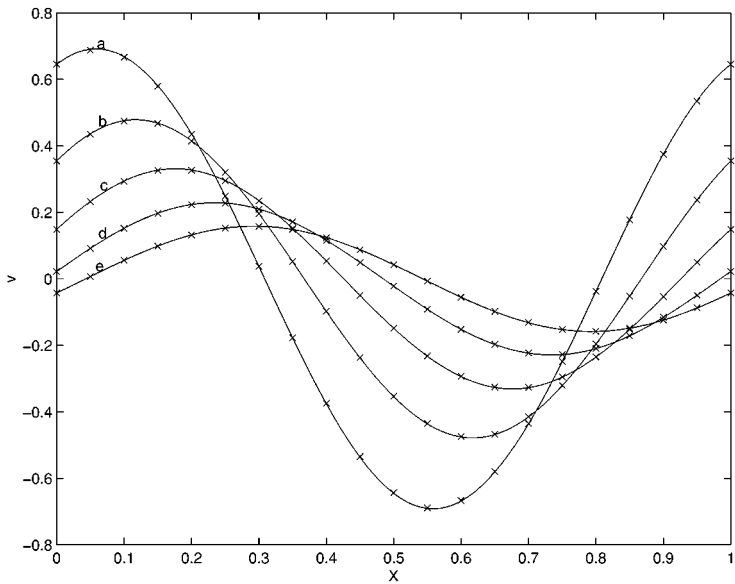


**FIG. 2.** Velocity profiles,  $v(x, 0.08\pi, t)$ , of unsteady decaying shear flow. Lattice size:  $8 \times 100$ .  $1/\tau = 0.95$ . Solid lines: analytic solutions.  $\times$ : simulation results. a:  $t = 0.3684211$ ; b:  $t = 0.7368421$ ; c:  $t = 1.105263$ ; d:  $t = 1.473684$ ; e:  $t = 1.842105$ .

where the summation is over the entire system, and  $\bar{u}$  is the analytic solution given by Eq. (3.2). In Table I,  $u$  and  $v$  are simulation results obtained using the incompressible LBGK model presented in this paper, and  $u_1$  and  $v_1$  are results by using He’s incompressible LBGK model [9]. In the simulation, the average pressure  $p_0$  of He’s model is set to be 3.0. Table I shows that the relative global errors produced by the model proposed in this paper vary slowly at different times, and they are much smaller than the errors produced by He’s model.

3.3. Driven Cavity Flow

Numerical simulations for the driven cavity flow have been studied by many authors using traditional schemes such as finite difference [5, 18] and multigrid [8, 19] methods. The lattice Boltzmann simulation was performed by Hou and Zou [12] with detailed analysis. The configuration of driven cavity flow considered here consists of a two-dimensional square cavity whose top plate moves from left to right with constant velocity, while the

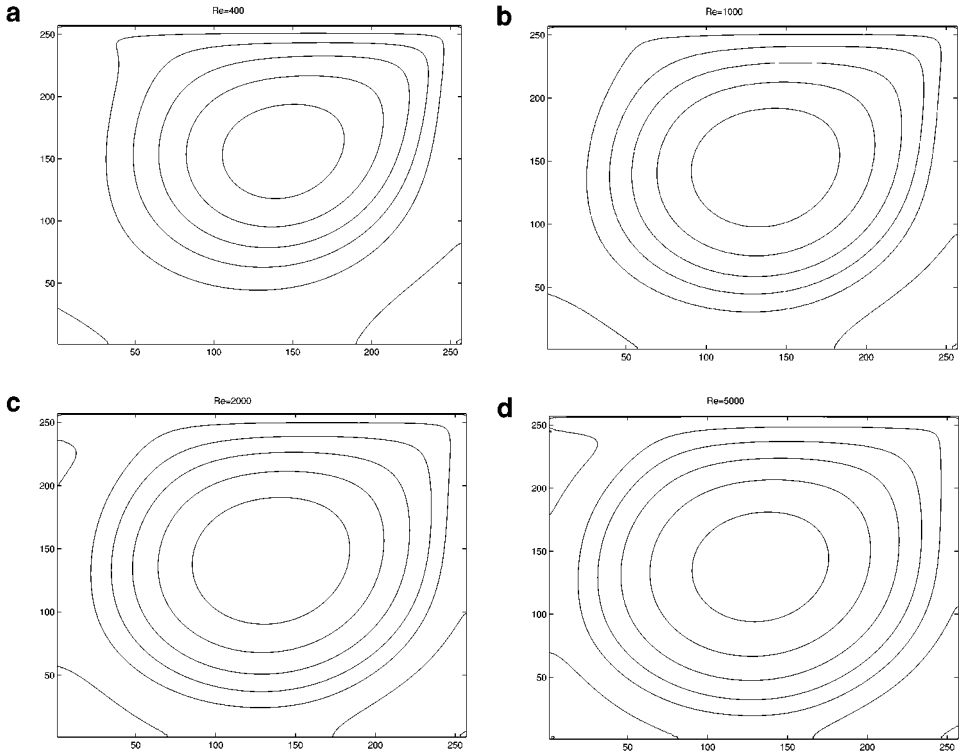
**TABLE I**  
**Relative Global Error of Velocity Field in 2-D Decaying Shear Flow**

	$t$				
	0.3684211	0.7368421	1.105263	1.473684	1.842105
$e(u) \times 10^4$	3.5252809	2.3628879	1.5602352	1.0394268	0.71491523
$e(v) \times 10^3$	2.5844411	2.5898510	2.5948778	2.5968753	2.5945725
$e(u_1) \times 10^3$	0.80553308	1.1336378	1.6208783	0.2162959	1.4642498
$e(v_1) \times 10^3$	3.8908607	7.2841784	14.286716	3.3058078	27.141689

other three boundaries are fixed. The fundamental characteristics of the driven cavity flow are the emergence of a large primary vortex in the center and of two secondary vortices in the lower two corners. The values of the stream function and the locations of the centers of the vortices are functions of the Reynolds number, which is determined by  $Re = LU/\nu$ , where  $L$  is the height or width of the cavity,  $U$  is the uniform velocity of the top plate, and  $\nu$  is the kinematic viscosity.

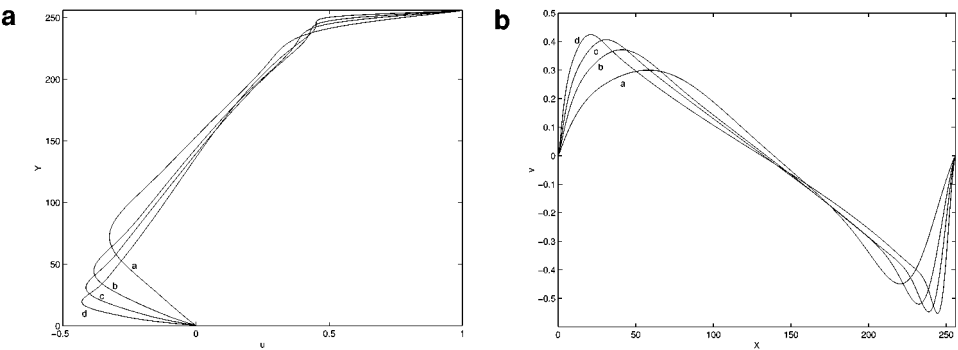
Numerical simulations are carried out using the present incompressible LBGK model for the driven cavity flow with  $Re = 400, 1000, 2000$ , and  $5000$  on a  $257 \times 257$  lattice. The relaxation parameter  $\omega = 1/\tau$  is set to be  $1.5, 1.75, 1.85$ , and  $1.85$ , respectively. The flow with  $Re = 400$  is first simulated, where the initial condition is set as  $u = v = 0, p = 1$ . The simulations for  $Re = 1000, 2000$ , and  $5000$  start from the steady states for  $Re = 400, 1000$ , and  $2000$ , respectively. In the simulations, steady state is reached when the difference between the velocities at the center of the cavity for successive  $1,000$  steps is less than  $5 \times 10^{-6}$ .

Figure 3 shows the contours of the stream function of the flow for the Reynolds numbers considered. The stream function,  $\psi$ , is defined as  $\psi = \int v dx - u dy$ , and is calculated from the discrete velocity field obtained from the LBGK simulation. In this paper, the integral is calculated in the  $y$  direction using the Simpson's rule with zero value on the bottom boundary. These plots show clearly the effect of the Reynolds number on the flow pattern. For low  $Re (\leq 1000)$ , only three vortices appear in the cavity, a primary one near the center and a pair of secondary ones in the lower corners of the cavity. At  $Re = 2000$ , a third secondary vortex is seen in the upper left corner. When  $Re$  reaches to  $5000$ , a tertiary



**FIG. 3.** Streamlines of the driven cavity flow for different Reynolds numbers. (a)  $Re = 400$ ; (b)  $Re = 1000$ ; (c)  $Re = 2000$ ; (d)  $Re = 5000$ .





**FIG. 4.** The velocity components,  $u$  and  $v$ , along the vertical and horizontal lines through the cavity center for the driven cavity flow at different Reynolds numbers. (a)  $Re = 400$ ; (b)  $Re = 1000$ ; (c)  $Re = 2000$ ; (d)  $Re = 5000$ .

vortex appears in the lower right corner. We can also see that the center of the primary vortex moves toward the center of the cavity as  $Re$  increases. The velocity components,  $u$  and  $v$ , along the vertical and horizontal center lines for different  $Re$  are shown in Fig. 4. The profiles are found to become near linear in the center core of the cavity as  $Re$  becomes large. These observations show that the present LBGK simulation is in agreement with the previous studies [8, 12, 18, 19].

To quantify the results, the strength and locations of the primary center vortex and the two secondary ones are listed in Table II. From the table, we can see that the strength and locations of the vortices predicted by the LBGK model agree well with those of previous work for all the Reynolds numbers considered. The velocity components along the vertical and horizontal lines through the cavity center are also compared with Ghia’s benchmark solutions [8]; the maximum, average, and relative global error are listed in Table III. Here the relative global

**TABLE II**  
**Strength and Locations of Vortex of the Driven Cavity Flow: ( $\cdot$ )<sub>c</sub> Primary Vortex; ( $\cdot$ )<sub>l</sub> Lower Left Vortex; ( $\cdot$ )<sub>r</sub> Lower Right Vortex**

Re		$\psi_c$	$x_c$	$y_c$	$\psi_l$	$x_l$	$y_l$	$\psi_r$	$x_r$	$y_r$
400	a	0.1136	0.5563	0.6000	$-1.46e-5$	0.0500	0.0500	$-6.45e-4$	0.8875	0.1188
	b	0.1139	0.5547	0.6055	$-1.42e-5$	0.0508	0.0469	$-6.42e-4$	0.8906	0.1250
	c	0.1121	0.5608	0.6078	$-1.30e-5$	0.0549	0.0510	$-6.19e-4$	0.8902	0.1255
	d	0.1126	0.5547	0.6094	$-1.36e-5$	0.0508	0.0469	$-6.23e-4$	0.8867	0.1250
1000	a	0.1173	0.5438	0.5625	$-2.24e-4$	0.0750	0.0813	$-1.74e-3$	0.8625	0.1063
	b	0.1179	0.5313	0.5625	$-2.31e-4$	0.0859	0.0781	$-1.75e-3$	0.8594	0.1094
	c	0.1178	0.5333	0.5647	$-2.22e-4$	0.0902	0.0784	$-1.69e-3$	0.8667	0.1137
	d	0.1170	0.5313	0.5625	$-2.21e-4$	0.0859	0.0781	$-1.68e-3$	0.8672	0.1172
2000	a	0.1116	0.5250	0.5500	$-6.90e-4$	0.0875	0.1063	$-2.60e-3$	0.8375	0.0938
	c	0.1204	0.5255	0.5490	$-7.26e-4$	0.0902	0.1059	$-2.44e-3$	0.8471	0.0980
	d	0.1186	0.5234	0.5469	$-7.13e-4$	0.0898	0.1016	$-2.40e-3$	0.8438	0.1016
5000	a	0.0921	0.5125	0.5313	$-1.67e-3$	0.0625	0.1563	$-5.49e-3$	0.8500	0.0813
	b	0.1190	0.5117	0.5352	$-1.36e-3$	0.0703	0.1367	$-3.08e-3$	0.8086	0.0742
	c	0.1214	0.5176	0.5373	$-1.35e-3$	0.0784	0.1373	$-3.03e-3$	0.8078	0.0745
	d	0.1120	0.5159	0.5391	$-1.29e-3$	0.0781	0.1328	$-2.85e-3$	0.8086	0.0781

Note. a, Vanka [19]; b, Ghia *et al.* [8]; c, Hou and Zou [12]; d, present work.

**TABLE III**  
**Errors of the Velocity Components through the Cavity Center:  $e_{\max}$ ,  
Maximum Error;  $e_{\text{ave}}$ , Average Error;  $e_{\text{rg}}$ , Relative Global Error**

		Re		
		400	1000	5000
$u(L/2, y)$	$e_{\max}$	$1.346 \times 10^{-2}$	$2.266 \times 10^{-2}$	$1.884 \times 10^{-2}$
	$e_{\text{ave}}$	$4.280 \times 10^{-3}$	$5.942 \times 10^{-3}$	$9.877 \times 10^{-3}$
	$e_{\text{rg}}$	$1.450 \times 10^{-2}$	$2.219 \times 10^{-2}$	$2.818 \times 10^{-2}$
$v(x, L/2)$	$e_{\max}$	$3.837 \times 10^{-3}$	$4.976 \times 10^{-3}$	$2.405 \times 10^{-2}$
	$e_{\text{ave}}$	$2.268 \times 10^{-3}$	$1.413 \times 10^{-3}$	$1.047 \times 10^{-2}$
	$e_{\text{rg}}$	$1.027 \times 10^{-2}$	$6.075 \times 10^{-3}$	$3.258 \times 10^{-2}$

error is calculated as in Eq. (3.3) with  $\bar{u}$  replaced by Ghia's benchmark solutions, and the summation is over the corresponding lines. The relative global errors about these velocity components are found to be less than 3.3% for all values of Re (data for Re = 2000 were not given in [8]) in comparison with Ghia's benchmark solutions. This indicates that the agreement between the present LBGK solutions and Ghia's benchmark solutions [8] is satisfactory.

### 3.4. Flow Around a Circular Cylinder

Although the flow in the square cavity is complex, the geometry is nevertheless simple because only flat boundaries are involved. To demonstrate the capability of the present incompressible LBGK model, we apply the model to the two-dimensional flow past a circular cylinder. The flow has been studied using lattice Boltzmann methods based on uniform meshes [3, 11, 20, 21] or nonuniform meshes [6, 10, 15] by several groups.

The cylinder is set into a channel with uniform velocity  $U$  at the inlet in the streamwise direction  $x$ , with origin at the center of the cylinder. The computation domain considered here is  $-2.5D \leq x \leq 11.5D$  and  $-3.5D \leq y \leq 3.5D$ , where  $D$  is the diameter of the cylinder. The boundary conditions are as follows:

inlet

$$u = U, v = 0$$

outlet

$$\frac{\partial u}{\partial x} = \frac{\partial v}{\partial x} = 0$$

top and bottom

$$\frac{\partial u}{\partial y} = 0, v = 0$$

solid surface of the cylinder

$$u = v = 0.$$

The Reynolds number ( $Re = DU/\nu$ ) of the flow is based on the uniform inlet velocity  $U$  and the cylinder diameter  $D$ . Numerical simulations are carried out for steady flow with

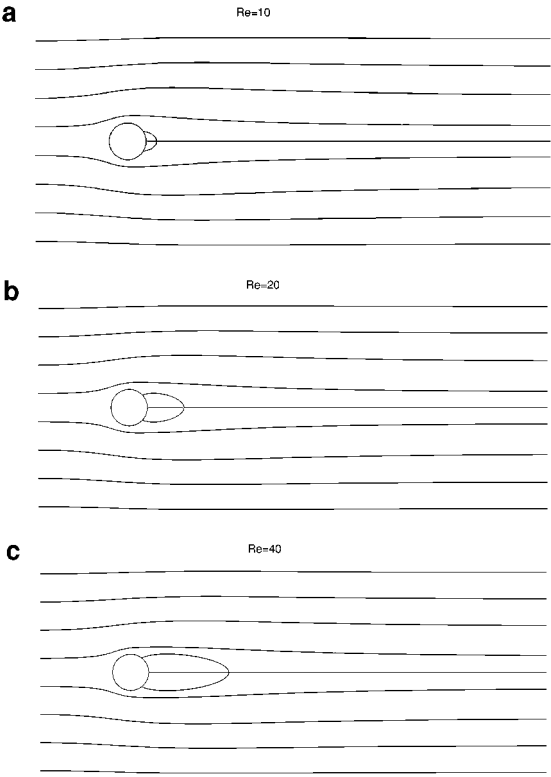


**FIG. 5.** Streamlines of the steady flow around a circular cylinder for different Reynolds numbers.

small Reynolds numbers ( $Re = 10, 20, 40$ ) and unsteady flow with  $Re = 82.67$  based on an  $N_y \times N_x = 211 \times 421$  grid. In the simulations, the surface of the circular cylinder is approximated by the lattice nodes closest to it. The relaxation parameter  $\omega = 1/\tau$  is set to be 0.7 for  $Re = 10$ , 1.2 for  $Re = 20$  and 40, and 1.6 for  $Re = 82.67$ , respectively.

Figure 5 shows the streamlines of the flow when it reaches its final steady state. In all cases, a pair of stationary recirculating eddies appear behind the cylinder. The wake length,  $L$ , the distance from the rearmost point of the cylinder to the end of the wake, and the separation angle,  $\theta$ , are measured. The quantitative geometrical parameters are listed in Table IV as well as related previous computational and experimental data. Both the wake length and the separation angle agree well with the results of previous studies for all the three Reynolds numbers considered.

For  $Re = 82.67$ , a lattice with larger size should be used. However, we still use the  $211 \times 421$  lattice because of limited computer resources. In the simulation, a periodic vortex shedding flow is obtained after a sufficient number of iterations. Figure 6 shows the instantaneous streamlines at different times within a cycle of the periodic vortex shedding.

For comparison, this flow is also simulated using He’s model [9] with the same lattice parameters and boundary conditions. A final periodic vortex shedding flow is also obtained, which is quite similar to the present incompressible LBGK solution. Figures 7 and 8 show the instantaneous pressure fields and the velocity components along the horizontal and vertical lines through the cylinder center. Close agreement between the two LBGK solutions can be observed from these figures. Table V lists the maximum, average, and relative global errors of the velocity components corresponding to Fig. 8. The relative global errors for the

**TABLE IV**  
**Geometrical Parameter of Flow around Circular Cylinder**

	Re					
	10		20		40	
	$2L/D$	$\theta$	$2L/D$	$\theta$	$2L/D$	$\theta$
a	0.434	27.96	1.786	43.37	4.357	53.34
b	0.68	32.5	1.86	44.8	4.26	53.5
c	0.474	26.89	1.842	42.9	4.490	52.84
d	0.498	30.0	1.804	42.1	4.38	50.12
e	0.533	31.61	1.867	42.27	4.400	53.13

*Note.* a, Nieuwstadt and Keller [16]; b, Coutanceau and Bouard [4]; c, He and Doolen [10]; d, Mei and Shyy [15]; e, present work.

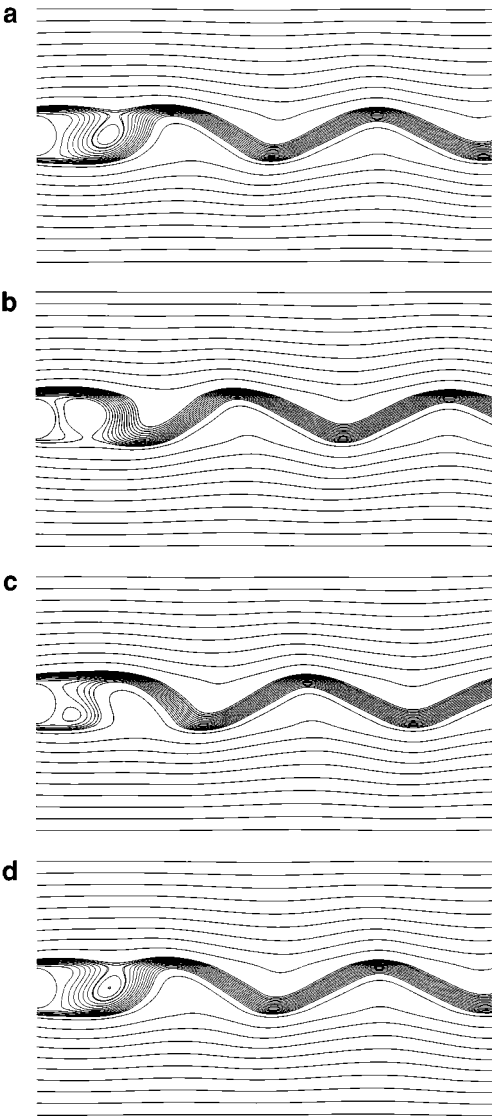


**FIG. 6.** Instantaneous streamlines of the flow around a circular cylinder for  $Re = 82.67$ .

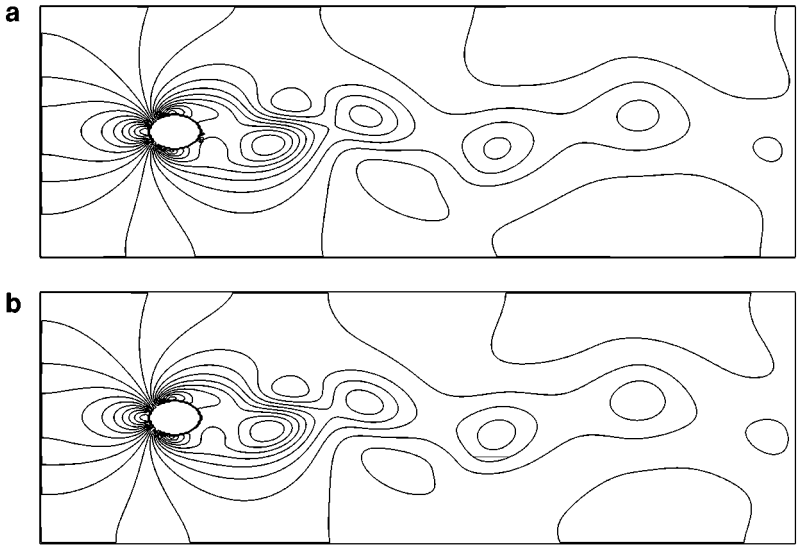


**FIG. 7.** Comparison of the pressure fields of the flow around a circular cylinder. (a) Present work; (b) He's [9] model.

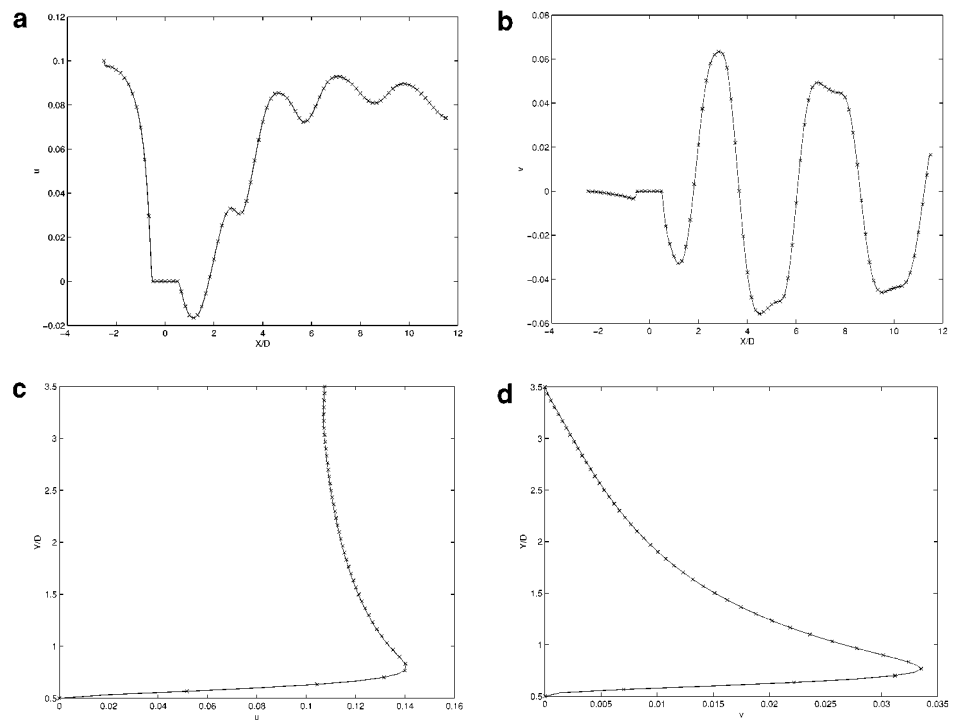


**FIG. 8.** Comparison of the velocity components of the flow around a circular cylinder. (a)  $u(x, 0)$ ; (b)  $v(x, 0)$ ; (c)  $u(0, y)$ ; (d)  $v(0, y)$ . Solid lines: He's model;  $\times$ : Present work.

**TABLE V**  
**Errors of the Velocity Components through the Cylinder Center:  $e_{\max}$ ,  
Maximum Error;  $e_{\text{ave}}$ , Average Error;  $e_{\text{rg}}$ , Relative Global Error**

	$u(x, 0)$	$v(x, 0)$	$u(0, y)$	$v(0, y)$
$e_{\max}$	$2.5614 \times 10^{-3}$	$1.6127 \times 10^{-3}$	$3.0158 \times 10^{-4}$	$1.0618 \times 10^{-4}$
$e_{\text{ave}}$	$8.2109 \times 10^{-4}$	$5.8597 \times 10^{-4}$	$1.0825 \times 10^{-4}$	$4.2629 \times 10^{-5}$
$e_{\text{rg}}$	$1.5685 \times 10^{-2}$	$2.1428 \times 10^{-2}$	$1.2034 \times 10^{-3}$	$3.9605 \times 10^{-3}$

velocity components are found to be less than 2.2% between the simulation results of the present LBGK model and He's model [9].

#### 4. SUMMARY AND CONCLUSION

In the above sections, a LBGK model for incompressible flows has been developed. Through multiscaling expansion, the Navier–Stokes equations are precisely recovered from the model accurate to the order of  $O(\epsilon^2)$  in the continuity equation and  $O(\epsilon^2 + \epsilon M^2)$  in the momentum equation. By choosing the distribution function appropriately, the compressible effect is eliminated in the incompressible LBGK model.

Numerical simulations are performed to test the performance of the incompressible LBGK model. The test problems include the plane Poiseuille flow condition, the unsteady shear decaying flow, the driven cavity flow, and the flow around a circular cylinder. For the steady plane Poiseuille flow with constant pressure gradient boundary condition, the simulation results agree well with the analytic solution of the incompressible Navier–Stokes equations.

As to the unsteady decaying shear flow, simulation is measured at several different times, and all of the results are in excellent agreement with the analytic solutions of the problem. The relative global errors of the results are also measured to compare the incompressible LBGK model presented in this paper with He's model [9]. It shows that our model has better performance than He's in dealing with this problem. The reason might be that our model completely eliminates the compressible effect, whereas He's model only reduces it. Another advantage of our model is that the average pressure does not need to be specified in advance; this enables us to use the model for general incompressible flows.

For the driven cavity flow, simulation is carried out with four different Reynolds numbers. The LBGK model correctly predicts the emergence of the third secondary vortex near the upper left corner for  $\text{Re} = 2000$  and the tertiary vortex in the lower right corner for  $\text{Re} = 5000$ . The strength and locations of the primary and two secondary vortices in the cavity are measured. Compared with the results of previous studies, the LBGK simulation for the driven cavity flow is satisfactory.

For flow around a circular cylinder, steady-state solutions are obtained for  $\text{Re} = 10, 20$ , and  $40$ . The wake length and separation angle of the steady flow agree well with previous experimental and computational data. For  $\text{Re} = 82.67$ , the present model predicts the periodic vortex shedding flow, and the simulation results are in excellent agreement with those obtained from He's model for the same problem.

The results of these numerical tests indicates the capability of the present incompressible LBGK model in handling steady and unsteady flows. The close agreement with the analytic solutions or experimental or computational data of previous studies shows the good

performance of the model. In conclusion, we have developed a LBGK model for the incompressible Navier–Stokes equations. The model completely eliminates the compressibility effect that lies in other existing LBGK models and can be used for both steady and unsteady flows.

## APPENDIX: RECOVERING THE INCOMPRESSIBLE NAVIER–STOKES EQUATIONS

It is well known that in incompressible flows,

$$O(\delta p) = O(\delta \rho) = O(M^2) \quad (\text{A1a})$$

$$O(\mathbf{u}) = O(M) \quad (\text{A1b})$$

in the limit  $M \rightarrow 0$ , where  $\delta p$  and  $\delta \rho$  are the pressure and density fluctuations, respectively.

To derive the incompressible Navier–Stokes equations from the LBGK model presented in this paper, we first expand the distribution function as

$$g_i = g_i^{(0)} + \epsilon g_i^{(1)} + \epsilon^2 g_i^{(2)} + \cdots, \quad (\text{A2})$$

where  $\epsilon = \Delta t$ . From Eqs. (2.10) and (2.11), we know that

$$\sum_{i=0}^8 g_i^{(m)} = 0 \quad (\text{A3a})$$

$$\sum_{i=0}^8 c \mathbf{e}_i g_i^{(m)} = \mathbf{0} \quad (\text{A3b})$$

for  $m = 1, 2, \dots$

With the multiscale expansion (A2), the evolution equation (2.12) of the incompressible LBGK model can be written in continuous form as

$$D_i g_i^{(0)} + \epsilon \left( \frac{1}{2} D_i^2 g_i^{(0)} + D_i g_i^{(1)} \right) + O(\epsilon^2) = -\frac{1}{\tau} g_i^{(1)}, \quad (\text{A4})$$

where  $D_i = \left( \frac{\partial}{\partial t} + c \mathbf{e}_i \cdot \nabla \right)$ . And therefore,

$$g_i^{(1)} = -\tau D_i g_i^{(0)} + O(\epsilon). \quad (\text{A5})$$

Applying Eq. (A5) to the left hand of Eq. (A4), we can rewrite Eq. (A4) as

$$D_i g_i^{(0)} = -\frac{1}{\tau} g_i^{(1)} + \epsilon \left( \tau - \frac{1}{2} \right) D_i^2 g_i^{(0)} + O(\epsilon^2). \quad (\text{A6})$$

Note that  $\mathbf{E}^{(2n+1)} = 0$  for  $n = 0, 1, \dots$ , where  $\mathbf{E}^{(n)}$  are the tensors defined as  $\mathbf{E}^{(n)} = \sum_{\alpha} \mathbf{e}_{\alpha 1} \mathbf{e}_{\alpha 2} \cdots \mathbf{e}_{\alpha n}$ , and

$$\sum_{i=1}^4 \mathbf{e}_{i\alpha} \mathbf{e}_{i\beta} = 2\delta_{\alpha\beta} \quad (\text{A7a})$$

$$\sum_{i=5}^8 \mathbf{e}_{i\alpha} \mathbf{e}_{i\beta} = 4\delta_{\alpha\beta} \quad (\text{A7b})$$

$$\sum_{i=1}^4 \mathbf{e}_{i\alpha} \mathbf{e}_{i\beta} \mathbf{e}_{i\zeta} \mathbf{e}_{i\theta} = 2\delta_{\alpha\beta\zeta\theta} \quad (\text{A7c})$$

$$\sum_{i=5}^8 \mathbf{e}_{i\alpha} \mathbf{e}_{i\beta} \mathbf{e}_{i\zeta} \mathbf{e}_{i\theta} = 4\Delta_{\alpha\beta\zeta\theta} - 8\delta_{\alpha\beta\zeta\theta}, \quad (\text{A7d})$$

where  $\delta_{\alpha\beta}$  and  $\delta_{\alpha\beta\zeta\theta}$  are the Kronecker tensors, and

$$\Delta_{\alpha\beta\zeta\theta} = \delta_{\alpha\beta}\delta_{\zeta\theta} + \delta_{\alpha\zeta}\delta_{\beta\theta} + \delta_{\alpha\theta}\delta_{\beta\zeta}. \quad (\text{A8})$$

With these identical equations, we obtain the moments of  $g_i^{(0)}$ :

$$\sum_i g_i^{(0)} = 0 \quad (\text{A9a})$$

$$\sum_i c\mathbf{e}_i g_i^{(0)} = \mathbf{u} \quad (\text{A9b})$$

$$\Pi^{(0)} =: \sum_i c^2 \mathbf{e}_i \mathbf{e}_i g_i^{(0)} = \mathbf{u}\mathbf{u} + pI \quad (\text{A9c})$$

$$\Gamma_{\alpha\beta\zeta}^{(0)} =: \sum_i c^3 \mathbf{e}_{i\alpha} \mathbf{e}_{i\beta} \mathbf{e}_{i\zeta} g_i^{(0)} = \frac{c^2}{3} (\delta_{\alpha\beta} \mathbf{u}_\zeta + \delta_{\alpha\zeta} \mathbf{u}_\beta + \delta_{\beta\zeta} \mathbf{u}_\alpha). \quad (\text{A9d})$$

With the aids of Eqs. (A9), the moments of Eq. (A6),

$$\sum_i D_i g_i^{(0)} = \epsilon \left( \tau - \frac{1}{2} \right) \sum_i D_i^2 g_i^{(0)} + O(\epsilon^2) \quad (\text{A10a})$$

and

$$\sum_i c\mathbf{e}_i D_i g_i^{(0)} = \epsilon \left( \tau - \frac{1}{2} \right) \sum_i c\mathbf{e}_i D_i^2 g_i^{(0)} + O(\epsilon^2), \quad (\text{A10b})$$

lead to the Euler equations,

$$\nabla \cdot \mathbf{u} = 0 + O(\epsilon) \quad (\text{A11a})$$

$$\frac{\partial \mathbf{u}}{\partial t} + \nabla \cdot \Pi^{(0)} = 0 + O(\epsilon), \quad (\text{A11b})$$

to the  $O(\epsilon)$  order, and the following equations,

$$\nabla \cdot \mathbf{u} = \epsilon \left( \tau - \frac{1}{2} \right) \mathbf{P} + O(\epsilon^2) \quad (\text{A12a})$$

$$\frac{\partial \mathbf{u}}{\partial t} + \nabla \cdot \Pi^{(0)} = \epsilon \left( \tau - \frac{1}{2} \right) \mathbf{Q} + O(\epsilon^2), \quad (\text{A12b})$$

to the  $O(\epsilon^2)$  order, where

$$\mathbf{P} = \sum_i D_i^2 g_i^{(0)} = \frac{\partial}{\partial t} (\nabla \cdot \mathbf{u}) + \nabla \cdot \left( \frac{\partial \mathbf{u}}{\partial t} + \nabla \cdot \Pi^{(0)} \right) = O(\epsilon)$$



and

$$\begin{aligned}
\mathbf{Q} &= \sum_i c \mathbf{e}_i D_i^2 g_i^{(0)} = \frac{\partial}{\partial t} \left( \frac{\partial \mathbf{u}}{\partial t} + \nabla \cdot \Pi^{(0)} \right) + \nabla \cdot \left( \frac{\partial \Pi^{(0)}}{\partial t} + \nabla \cdot \Gamma^{(0)} \right) \\
&= O(\epsilon) + \nabla \cdot \left( \frac{\partial \Pi^{(0)}}{\partial t} \right) + \frac{c^2}{3} (\nabla^2 \mathbf{u} + 2 \nabla (\nabla \cdot \mathbf{u})) \\
&= O(\epsilon) + \nabla \cdot \left( \frac{\partial p}{\partial t} + \frac{\partial (\mathbf{u} \mathbf{u})}{\partial t} \right) + \frac{c^2}{3} (\nabla^2 \mathbf{u}) \\
&= O(\epsilon) + O(M^2) + \frac{c^2}{3} (\nabla^2 \mathbf{u}).
\end{aligned}$$

The term  $\frac{\partial p}{\partial t} + \frac{\partial (\mathbf{u} \mathbf{u})}{\partial t}$  is of order  $O(M^2)$  due to Eqs. (A1). By applying the above results about  $P$  and  $Q$  to Eqs. (A12), the incompressible Navier–Stokes equations are derived accurate to the order of  $O(\epsilon^2)$  in the continuity equation and  $O(\epsilon^2 + \epsilon M^2)$  in the momentum equation

$$\nabla \cdot \mathbf{u} = 0 + O(\epsilon^2) \quad (\text{A13a})$$

$$\frac{\partial \mathbf{u}}{\partial t} + \nabla \cdot (\mathbf{u} \mathbf{u}) = -\nabla p + \nu \nabla^2 \mathbf{u} + O(\epsilon^2 + \epsilon M^2), \quad (\text{A13b})$$

where the kinematic viscosity is determined by

$$\nu = \frac{(2\tau - 1) (\Delta x)^2}{6 \Delta t}. \quad (\text{A14})$$

Now we discuss how to compute the pressure  $p$  from the distribution function. According to the expression of  $g_0^{(0)}$ , we have

$$\begin{aligned}
\frac{4\sigma}{c^2} p(\mathbf{x}, t + \epsilon) &= -g_0^{(0)}(\mathbf{x}, t + \epsilon) + s_0(\mathbf{u}(\mathbf{x}, t + \epsilon)) \\
&= -g_0(\mathbf{x}, t + \epsilon) + \epsilon g_0^{(1)}(\mathbf{x}, t + \epsilon) + s_0(\mathbf{u}(\mathbf{x}, t + \epsilon)) \\
&= -g_0(\mathbf{x}, t + \epsilon) + \epsilon g_0^{(1)}(\mathbf{x}, t) + s_0(\mathbf{u}(\mathbf{x}, t + \epsilon)) + \epsilon^2 \frac{\partial g_0^{(1)}}{\partial t} \\
&= -g_0(\mathbf{x}, t + \epsilon) + \epsilon g_0^{(1)}(\mathbf{x}, t) + s_0(\mathbf{u}(\mathbf{x}, t + \epsilon)) + O(\epsilon^2),
\end{aligned}$$

while the term  $\epsilon g_0^{(1)}(\mathbf{x}, t)$  can be neglected because from the evolution equation we have

$$\begin{aligned}
g_0^{(1)}(\mathbf{x}, t) &= -\frac{1}{\tau \epsilon} [g_0(\mathbf{x}, t + \epsilon) - g_0(\mathbf{x}, t)] \\
&= -\tau \left[ \frac{\partial g_0(\mathbf{x}, t)}{\partial t} + O(\epsilon) \right] \\
&= -\tau \left[ \frac{\partial g_0^{(0)}(\mathbf{x}, t)}{\partial t} + O(\epsilon) \right] \\
&= \tau \left[ 4\sigma \frac{\partial p(\mathbf{x}, t)}{\partial t} - \frac{\partial s_0(\mathbf{u}(\mathbf{x}, t))}{\partial t} \right] + O(\epsilon).
\end{aligned}$$

Note that  $\frac{\partial p}{\partial t} = O(M^2)$  and  $s_0(\mathbf{u}) = O(|\mathbf{u}|)^2 = O(M^2)$ , so  $g_0^{(1)}(\mathbf{x}, t) = O(\epsilon + M^2)$ . Therefore,

$$\frac{4\sigma}{c^2} p(\mathbf{x}, t + \epsilon) = -g_0(\mathbf{x}, t + \epsilon) + s_0(\mathbf{u}(\mathbf{x}, t + \epsilon)) + O(\epsilon^2 + \epsilon M^2) \quad (\text{A15a})$$

or

$$\frac{4\sigma}{c^2} p(\mathbf{x}, t + \epsilon) = \sum_{i=1}^8 g_i(\mathbf{x}, t + \epsilon) + s_0(\mathbf{u}(\mathbf{x}, t + \epsilon)) + O(\epsilon^2 + \epsilon M^2) \quad (\text{A15b})$$

due to Eqs. (2.10) and (A9a). As a result, the pressure  $p$  can be computed as

$$p = \frac{c^2}{4\sigma} \left[ \sum_{i=1}^8 g_i + s_0(\mathbf{u}) \right] \quad (\text{A16})$$

with accuracy of order  $O(\epsilon^2 + \epsilon M^2)$ , which is consistent with the order of the incompressible Navier–Stokes equations (A13).

## ACKNOWLEDGMENTS

The author Zhaoli Guo thanks Professor Haiping Fang for his helpful discussions. We also thank the reviewers for comments which greatly improved the work. This work is supported in part by the National Key Project of Fundamental Research, the Ministry of Science and Technology, People's Republic of China (Grant G1999022207), and the National Science Foundation (Grant 59676030).

## REFERENCES

1. Reference removed in proofs.
2. S. Chen and G. Doolen, Lattice Boltzmann method for fluid flows, *Ann. Rev. Fluid Mech.* **30**, 329 (1998).
3. S. Chen, D. Martinez, and R. Mei, On boundary conditions in lattice Boltzmann methods, *Phys. Fluids* **8**, 2527 (1996).
4. M. Coutanceau and R. Bouard, Experimental determination of the main features of the viscous flow in the wake of a circular cylinder in uniform translation. 1. Steady flow, *J. Fluid Mech.* **79**, 231 (1977).
5. W.-N. E, and J. Liu, Essential compact scheme for unsteady viscous incompressible flows, *J. Comput. Phys.* **126**, 122 (1996).
6. O. Filippova and D. Hänel, Grid refinement for lattice-BGK models, *J. Comput. Phys.* **147**, 219 (1998).
7. U. Frisch, D. d'Humières, B. Hasslacher, P. Lallemand, Y. Pomeau, and J.-P. Rivet, Lattice gas hydrodynamics in two and three dimensions. *Complex Syst.* **1**, 649 (1987).
8. U. Ghia, K. N. Ghia, and C. T. Shin, High-Re solutions for incompressible flow using the Navier–Stokes equations and a multigrid method, *J. Comput. Phys.* **48**, 387 (1982).
9. X. He and L.-S. Luo, Lattice Boltzmann model for the incompressible Navier–Stokes equation, *J. Stat. Phys.* **88**, 927 (1997).
10. X. He and G. Doolen, Lattice Boltzmann method on curvilinear coordinates system: Flow around a circular cylinder, *J. Comput. Phys.* **134**, 306 (1997).
11. F. J. Higuera and S. Succi, Simulating the flow around a circular cylinder with a lattice Boltzmann equation, *Europhys. Lett.* **8**, 517 (1989).
12. S. Hou and Q. Zou, Simulation of cavity flow by the lattice Boltzmann method, *J. Comput. Phys.* **118**, 329 (1995).

13. Z. Lin, H. Fang, and R. Tao, Improved lattice Boltzmann model for incompressible two-dimensional steady flows, *Phys. Rev. E* **54**, 6323 (1997).
14. D. O. Martinez, W. H. Matthaeus, S. Chen, and D. C. Montgomery, Comparison of spectral method and lattice Boltzmann simulations of two-dimensional hydrodynamics, *Phys. Fluids*. **6**, 1285 (1994).
15. R. Mei and Q. Shyy, On the finite difference-based lattice Boltzmann method in curvilinear coordinates, *J. Comput. Phys.* **143**, 426 (1998).
16. F. Nieuwstadt and H. B. Keller, Viscous flow past circular cylinders, *Comput. Fluids*. **1**, 59 (1973).
17. Y. Qian, D. d'Humières, and P. Lallemand, Lattice BGK models for Navier–Stokes equation, *Europhys. Lett.* **17**, 479 (1992).
18. R. Schreiber and H. Keller, Driven cavity flow by efficient numerical techniques, *J. Comput. Phys.* **49**, 310 (1983).
19. S. P. Vanka, Block-implicit multigrid solution of Navier–Stokes equations in primitive variables, *J. Comput. Phys.* **65**, 138 (1986).
20. L. Wagner, Pressure in lattice Boltzmann simulations of flow around a cylinder, *Phys. Fluids*. **6**, 3516 (1994).
21. L. Wagner and F. Hayot, Lattice Boltzmann simulations of flow past a cylindrical obstacle, *J. Stat. Phys.* **81**, 63 (1995).
22. Q. Zou, S. Hou, S. Chen, and G. Doolen, An improved incompressible lattice Boltzmann model for time-independent flows, *J. Stat. Phys.* **81**, 35 (1995).